Review of
Scientific Instruments

# Frequency-domain hot-wire sensor and 3D model for thermal conductivity measurements of reactive and corrosive materials at high temperatures

Cite as: Rev. Sci. Instrum. **91**, 054904 (2020); https://doi.org/10.1063/1.5138915
Submitted: 15 November 2019 • Accepted: 23 April 2020 • Published Online: 14 May 2020

**M. C. Wingert, A. Z. Zhao, Y. Kodera, et al.**

AIP Publishing

Review of
Scientific Instruments

ARTICLE

scitation.org/journal/rsi

# Frequency-domain hot-wire sensor and 3D model for thermal conductivity measurements of reactive and corrosive materials at high temperatures

Cite as: Rev. Sci. Instrum. 91, 054904 (2020); doi: 10.1063/1.5138915
Submitted: 15 November 2019 • Accepted: 23 April 2020 •
Published Online: 14 May 2020

View Online Export Citation CrossMark

M. C. Wingert,[1] A. Z. Zhao,[1] Y. Kodera,[1] S. J. Obrey,[2] and J. E. Garay[1,a)]

AFFILIATIONS

[1] Materials Science and Engineering Program, Mechanical and Aerospace Engineering Department, University of California, San Diego, California 92093, USA

[2] Chemistry Division, Los Alamos National Laboratory, Los Alamos, New Mexico 87545, USA

[a)] Author to whom correspondence should be addressed: jegaray@ucsd.edu

## ABSTRACT

High temperature solids and liquids are becoming increasingly important in next-generation energy and manufacturing systems that seek higher efficiencies and lower emissions. Accurate measurements of thermal conductivity at high temperatures are required for the modeling and design of these systems, but commonly employed time-domain measurements can have errors from convection, corrosion, and ambient temperature fluctuations. Here, we describe the development of a frequency-domain hot-wire technique capable of accurately measuring the thermal conductivity of solid and molten compounds from room temperature up to 800 °C. By operating in the frequency-domain, we can lock into the harmonic thermal response of the material and reject the influence of ambient temperature fluctuations, and we can keep the probed volume below 1 $\mu$l to minimize convection. The design of the microfabricated hot-wire sensor, electrical systems, and insulating wire coating to protect against corrosion is covered in detail. Furthermore, we discuss the development of a full three-dimensional multilayer thermal model that accounts for both radial conduction into the sample and axial conduction along the wire and the effect of wire coatings. The 3D, multilayer model facilitates the measurement of small sample volumes important for material development. A sensitivity analysis and an error propagation calculation of the frequency-domain thermal model are performed to demonstrate what factors are most important for thermal conductivity measurements. Finally, we show thermal conductivity measurements including model data fitting on gas (argon), solid (sulfur), and molten substances over a range of temperatures.

## I. INTRODUCTION

The designs of next-generation energy and manufacturing systems increasingly rely on operation at high temperature for both the high efficiencies and energy densities inherent in higher quality heat sources. It is necessary in many system designs to both transport and store the captured heat using liquids or more accurately, molten compounds or melts. For efficient operation and cost control, the intrinsic heat transfer properties of these materials and melts must be accounted for in the overall design of high temperature systems.[1]

Potential next-generation concentrated solar power plants have various designs including harnessing heated falling solid particles, molten salts, or compressed gases to operate above 600 °C.[2] These higher temperatures allow the use of the supercritical $CO_2$ Brayton cycle[3,4] that has a higher electricity generation efficiency and smaller system size relative to that of a steam system, all at 1/10th of the cost. In addition to solar thermal power, advanced nuclear reactors are also being designed to utilize molten salts[5,6] and molten metals[7] as heat transfer fluids. The thermal properties of solid particles, molten salts, molten metals, and compressed gases at elevated temperatures will be critical in the design of next-generation energy sources. Enhancing the thermal conductivity of these high temperature heat transfer and thermal storage materials would further increase the power output of high temperature systems. Introducing nanosized particles into fluids to create nanofluids has been an attractive way to significantly increase thermal conductivity,[8–11] but there is still controversy over the mechanism of increased thermal conductivity as well as the practicality of nanofluids. Additionally, next-generation additive manufacturing of functional parts from powders using laser-based cladding and melting is also dependent on the high temperature properties of the precursor powders and melt pool. The heating rate, temperature profile, and solidification rate of additively manufactured parts, which are dictated by their high temperature thermal transport properties, determine the final microstructure and mechanical properties of the produced components.[12,13] Thus, accurate material thermal properties at high-temperature conditions and in various extreme material environments are important for numerous next-generation energy systems and manufacturing schemes.

One of the most widely used and long-held techniques to measure the thermal conductivity of gases, liquids, powders, and molten materials is transient hot-wire.[14,15] In this technique, the time-dependent temperature rise in a thin suspended metallic wire due to a step-change in voltage or current is measured and related to the thermal conductivity of the material surrounding that wire.[16–24] For simplicity, data analysis in most studies uses a linear relation between temperature rise and thermal conductivity arising from Fourier's law, assuming an infinitely long heat source with no thermal mass. This assumption, however, only approximates experimental results for a *short* time interval, given a careful experimental setup outside of which additional thermal losses must be accounted for in order to obtain accurate results, significantly complicating the thermal analysis.[25] In a real experiment, the measured temperature rise is affected at short times by the heat capacity of the heating wire itself and at longer times by the axial conduction along the wire (end-effects)[25,26] and convection in the surrounding fluid. To achieve linear temperature rises, experimental setups use long heating wires (often >1 m) to reduce temperature non-uniformity along the wire, large containment vessels to approximate semi-infinite surrounding fluid volumes, and short measurement time windows, usually only using data between 0.1 s and 1 s after applying heating current, to exclude self-heating and convection. In practice, the linear region used for data fitting is only identified by inspection[27] after the experiment is concluded, and deviation from linearity is assumed to be due to self-heating (short times, <0.1 s) and fluid convection or conduction through the container walls (longer times, >1 s).[28,29] Analysis providing the clear range and time bounds of this linear region requires either prerequisite knowledge of the thermal properties of the materials present in the experiment[25] or using a numerical algorithm to identify the linear range in the data without physical reasoning.[30,31] Time-domain thermal measurements are also unfortunately susceptible to noise and temperature errors originating from the ambient thermal environment, requiring carefully insulated and shielded experimental setups.

The development of frequency-domain thermal measurements, particularly the 3-omega (3ω) method,[32] has proven useful for removing such errors and obtaining very accurate thermal measurement properties of solids over wide temperature ranges. In the 3ω technique, temperature fluctuations of a long, thin Joule heated metal strip deposited on the sample surface are related to the heat flux dissipated in the sample.[33–36] Using an AC current (at 1ω frequency, $I_\omega$) to heat the metal strip induces resistance fluctuations at a second harmonic (2ω) and voltage fluctuations at a third harmonic (3ω, $V_{3\omega}$). The temperature fluctuations are then calculated via the temperature coefficient of resistance (TCR, $dT/dR$) of the heater element,

$$\tilde{T}_{2\omega,avg} = -2\frac{V_{3\omega}}{I_\omega}\left(\frac{dT}{dR}\right). \tag{1}$$

Operating thermal measurements in the frequency-domain offers many advantages over the time-domain, including reduction of $1/f$ noise while measuring higher frequency signals, reduction of thermally probed volumes, and rejection of ambient temperature gradients or fluctuations.

The 3ω method has primarily been used for characterizing solid materials although earlier specific heat spectroscopy studies[37–39] have shown the promise of frequency-domain techniques for investigating the properties of liquids and phase changes. More recent work has been done to extend 3ω method to liquids[40–42] and soft materials;[43] however, they still retain the basic geometry of the planar 3ω method that includes parasitic heat flux through the supporting substrate that usually has much higher thermal conductivity than the liquid or soft material being studied. In order to ensure as much of the generated heat flux propagates through the liquid sample, wire geometries immersed or embedded in the sample are ideal, limiting the parasitic conduction pathways to the wire axis itself. Such wire-like 3ω heater geometries have been used to study the wire itself,[44] gases and liquids,[45–52] as well as hybrid geometries such as metal-film coated glass wires.[53,54] Early 3ω hot-wire measurements, however, have been considered unreliable by transient hot-wire standards,[55] but this largely stems from over-simplified heat-transfer analysis for wire geometries in early frequency-domain hot-wire experiments, which did not take into account radial and axial heat conduction or the thermal mass of the heating wire.

In this work, we detail the design of a 3ω hot-wire sensor and thermal model to measure the thermal conductivity of gaseous, liquid, and solid phases of materials over extended temperature ranges. The sensor operates in the frequency-domain to reduce ambient thermal and 1/f noise and limit the thermally probed volume (<1 $\mu$l) to enable small sample batches and reduce convection effects. In addition, the sensor is designed to survive and operate at high temperatures (up to 800 °C) and in chemically harsh or corrosive environments (with the use of protective coatings when necessary). Next, we discuss the heat transfer analysis for a hot-wire in the frequency-domain starting from an infinitely long wire and extend this analysis to a full three-dimensional solution including axial conduction and thermal impedance due to surface coatings as well as appropriate use conditions. Finally, we show the experimental results on argon, silicone oil, ethanol, methanol, and water at room temperature as well as temperature-dependent measurements on sulfur through solid–solid and solid–liquid phase transitions, including analysis of error sources and propagation.

## II. EXPERIMENTAL SETUP AND DESIGN

The 3ω hot-wire sensor developed for this work [Fig. 1(a)] was designed to meet the following criteria: (1) be relatively simple to

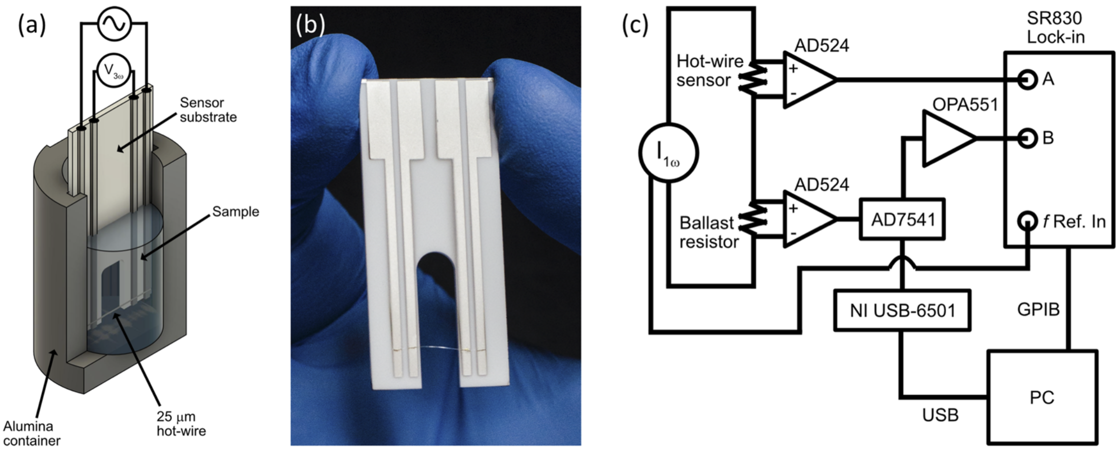

**FIG. 1**. (a) Sensor chip and sample measurement diagram, (b) fabricated hot-wire sensor on the chip, and (c) 3ω measurement electronics.

fabricate for mass production, (2) be able to measure small sample volumes (~5 ml) to enable rapid testing of small batch products, (3) be high-temperature (1000 K) compatible, and (4) be capable of measuring corrosive/reactive compounds. For criteria (1), the sensor was designed such that the parts could be mass manufactured with minimal material components to reduce possible reactions with sample materials. First, electrically insulating alumina ($Al_2O_3$) ceramic substrates were laser machined to specific dimensions [Fig. 1(b)], leaving a 5 mm wide gap open for the suspended hot-wire with extended prongs, allowing the sensor to rest on the bottom of the sample container. Pt electrical leads (~1 $\mu$m thick) were then sputtered onto alumina substrates with a thin Ti adhesion layer. 25 $\mu$m diameter Pt wire is then spot-welded to the Pt leads such that it is suspended between the two substrate prongs across the 5 mm spacing. Pt wire was chosen for its combination of electrical resistivity and temperature-coefficient-of-resistance (TCR), which results in Pt having a high $dR/dT$ compared to other metal wires (gold, silver, copper, aluminum, and tungsten). This makes Pt an ideal metallic wire material for short hot-wires. Finally, the sensor can be coated with an alumina film, either by CVD or ALD, to provide extra corrosion resistance and electrical insulation if needed for the sample being measured. This fabrication process is batch manufacturable and can be automated for sensor uniformity, while additionally allowing sensors to be disposable. Because this design uses only $Al_2O_3$, Ti (for the thin adhesion layer), and Pt and each sensor is annealed in a high-temperature furnace at 1200 K for 2 h prior to use for testing, the entire sensor can survive temperatures in excess of 1000 K. These materials also enable the sensors to operate in chemically harsh or corrosive environments although the use of protective alumina coatings (or other materials depending on chemistries involved) may be necessary as even Pt will react with some elements at high temperature.

For sample testing, the sensor is immersed within the sample in an alumina crucible [Fig. 1(a)]. The sensor is simply dipped into a liquid sample. Samples that are solids at room temperature can be measured by pouring powder or granular samples over the sensor. To measure fully dense solids at room-temperature, the sensor can be lowered into the sample after it has been heated above its melting point and then carefully cooled to solidify the sample around the wire and avoid breaking the thin platinum wire. The sensor and sample, all in the crucible, are placed inside a high-temperature furnace, which is then successively purged with argon gas to reduce the oxygen content before heating the sample. Tests can be performed in argon atmosphere or under light vacuum conditions.

The 3ω measurement is performed using the circuit shown in Fig. 1(c), where AC current ($I_{1\omega}$) is passed through the hot-wire, to heat the metal wire, and through a ballast resistor. Instrumentation amplifiers (AD524) measure the voltage drop across both the sensor and ballast resistors, and a multiplying DAC (AD75341) matches the ballast resistor voltage to the voltage across the sensor. By matching the ballast voltage to that of the sensor, spurious 3ω signals can be removed from the measurement, greatly increasing the 3ω signal-to-noise ratio. A lock-in amplifier (SR830) is then used to measure the third harmonic ($V_{3\omega}$) of the voltage difference between the sensor and ballast resistors.

镇流电阻

In previous 3ω hot-wire experiments,[45] only experimental data over truncated frequency ranges (after undergoing a transformation procedure) were used for fitting thermal conductivity in order to use linear fits with a simplified analytical model. For the short hot-wire lengths used in our sensors, however, it is difficult to decouple the effect of the thermal properties (thermal conductivity and heat capacity) of the wire and sample. Therefore, all measurements herein are performed over a frequency range of 1–1000 Hz, and no data are truncated. We use all data from this frequency range to fit to thermal models, detailed in Sec. III, and verify that the finite wire length model satisfactorily fits the data. It is important to note that fitting the models to measurements is very sensitive to the length of the hot-wire, and therefore, great care in measuring the length must be taken. We find that calculating the length from the four-point resistance of the wire, compared to a measured resistance-per-length from longer sections of the same wire as that used in the sensor, provides the most accurate wire length. Measurements were not done at frequencies lower than 1 Hz due to the very long stabilization times needed[45] or for frequencies above 1000 Hz because of the near-zero temperature rise. Heating currents ($I_{1\omega}$) of 80–100 mA were used for liquids to generate enough temperature rise ($\tilde{T}_{2\omega,avg}$) for a good signal-to-noise ratio due to the low hot-wire electrical resistance (~1.3 Ω), whereas only 30 mA was used for gases to limit the temperature rise to approximately the same observed for measurements in liquids. Thermal conductivity of the measured sample was then found by fitting the data with the finite-length model using least-squares. Uncertainties in other measured variables (wire diameter, length, thermal properties, and sample heat capacity) were used to find propagated error in the measurement for the fit thermal conductivity.

## III. HOT-WIRE HEAT TRANSFER ANALYSIS IN THE FREQUENCY-DOMAIN

To solve for the temperature distribution in the hot-wire measurement, we consider a suspended cylindrical wire of radius $r_0$ and length $L = 2l$ surrounded by a thermally conductive medium that extends very far away from the wire. This geometry is composed of two volumes with thermal conductivity, $\kappa_N$, density, $\rho_N$, and heat capacity, $C_N$: the suspended wire and the surrounding sample media, each denoted by the subscripts $N = 0$ and $N = 1$, respectively. The governing heat equation must account for heat conduction into the sample media (radial direction $r$) and along the conductive wire toward its anchor points (axial direction $z$),

$$\frac{\partial^2 T_N}{\partial r^2} + \frac{1}{r}\frac{\partial T_N}{\partial r} + \frac{\partial^2 T_N}{\partial z^2} + \frac{P_N'''}{\kappa_N} - \frac{\rho_N C_N}{\kappa_N}\frac{\partial T_N}{\partial t} = 0. \tag{2}$$

Assuming that the heat generated in the hot-wire is periodic and allowed to settle such that steady-state temperature oscillations are being measured, the temperature and heating power can be written in terms of sinusoids as $T_N(r,z,t) = \tilde{T}_N(r,z)e^{i2\omega t}$ and $P_N''' = \tilde{P}_N''' e^{i2\omega t}$, respectively, where the volumetric power dissipated in each region $N$ is the $\tilde{P}_0''' = \tilde{P}_0/\pi r_0^2 L$ and $\tilde{P}_{N\neq0}''' = 0$ with $\tilde{P}_0 = I_\omega^2 R$. Here, $\omega$ is the angular frequency of the AC heating current, with root-mean-square (rms) amplitude $I_\omega$, applied to the metal hot-wire, with electrical resistance $R$, and the resulting temperature oscillations due to Joule heating in the wire occur at frequency $2\omega$. The heat equation [Eq. (2)] can then be rewritten in terms of the temperature and power oscillation amplitudes,

$$\frac{\partial^2 \tilde{T}_N}{\partial r^2} + \frac{1}{r}\frac{\partial \tilde{T}_N}{\partial r} + \frac{\partial^2 \tilde{T}_N}{\partial z^2} + \frac{\tilde{P}_N'''}{\kappa_N} - \frac{i2\omega\rho_N C_N}{\kappa_N}\tilde{T}_N = 0. \tag{3}$$

Since the penetration depth of the temperature oscillations is much shorter than the extent of the surrounding sample media, we can assume that the sample is semi-infinite and the temperature at distances very far away from the wire ($r \to \infty$) is ambient. Furthermore, the wire is thermally anchored at its ends ($z = 0, 2l$) to electrical connections that act as heat sinks. The radial and axial boundary conditions taking symmetry into account are

$$\left.\frac{\partial \tilde{T}_0}{\partial r}\right|_{r=0} = \left.\tilde{T}_2\right|_{r\to\infty} = \left.\frac{\partial \tilde{T}_N}{\partial z}\right|_{z=l} = \left.\tilde{T}_N\right|_{z=0} = 0. \tag{4}$$

At the interface between each volume region, $N$, heat flux and temperature continuity must exist with the possibility of a finite non-zero discontinuity due to the interfacial thermal contact resistance, $\mathcal{R}_{N,N+1}$, between adjacent layers $N$ and $N + 1$,

$$-\kappa_N \left.\frac{\partial \tilde{T}_N}{\partial r}\right|_{r_N} = -\kappa_{N+1}\left.\frac{\partial \tilde{T}_{N+1}}{\partial r}\right|_{r_N} = \frac{1}{\mathcal{R}_{N,N+1}}\left[\left.\tilde{T}_N\right|_{r_N} - \left.\tilde{T}_{N+1}\right|_{r_N}\right]. \tag{5}$$

From this point, three common hot-wire geometry scenarios can be examined: Case 1 is the simplest where the un-coated wire is assumed to be of infinite length and axial heat loss is neglected, and this has almost always been assumed in previous work [Fig. 2(a)];

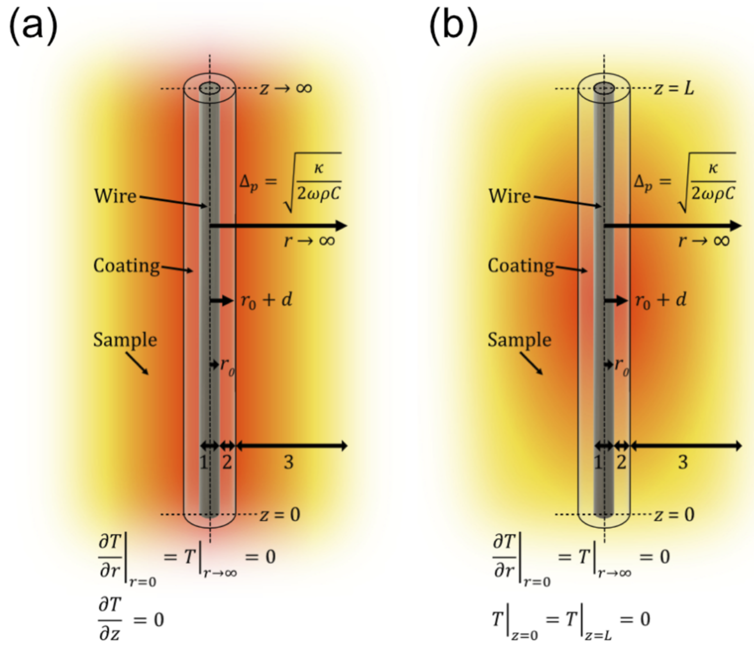

**FIG. 2**. Hot-wire models for (a) infinite and (b) finite length ($L$) wire cases including coating layer (coating thickness $d$) and radial ($r$) and axial ($z$) boundary conditions.

case 2 includes axial heat loss through the wire such that the finite length of the hot-wire itself is taken into account; and case 3 adds an electrically insulating coating of finite thickness to the hot-wire, separating it from the surrounding sample material, but also includes axial heat losses [Fig. 2(b)]. Analytical solutions for each of these cases are developed and discussed in Secs. III A–III C.

### A. Case 1: Neglecting axial conduction (infinitely long wire)

In the simplest case, axial conduction in Eq. (3) is ignored such that the wire is essentially of infinite length and the temperature along the wire is constant ($\partial^2 \tilde{T}_N/\partial z^2 = 0$), equivalent to Fig. 2(a) but without the wire coating ($d = 0$). With only the radial boundary conditions in Eq. (4) considered, the solution to this Bessel type equation is

$$\tilde{T}_N(r) = A_N I_0(q_N r) + B_N K_0(q_N r) + \left(\frac{\tilde{P}_N'''}{\kappa_N q_N^2}\right), \tag{6}$$

where $I_j(x)$ and $K_j(x)$ are the $j$-th order modified Bessel functions of the first and second kind, respectively, and the radial thermal wavevector is

$$q_N = \sqrt{\frac{i2\omega\rho_N C_N}{\kappa_N}} \tag{7}$$

of which the inverse is the radial thermal penetration depth, $|q_N| = 1/\Delta_{p,N}$. Therefore, the temperature rise decreases as the frequency of the heating current, $\omega$, increases due to the reduced $\Delta_{p,N}$, eventually being completely damped out (zero temperature rise). Conversely, as the frequency is lowered, the thermal penetration depth into the sample continuously increases.

Applying the radial boundary conditions from Eq. (4) leads to the following temperature profile solutions in the wire ($N = 0$) and sample ($N = 1$):

$$\tilde{T}_N(r) = \begin{cases} \tilde{T}_0(r) = A_0 I_0(q_0 r) + \frac{\tilde{P}_0}{\pi r_0^2 L \kappa_0 q_0^2} & 0 \le r \le r_0 \\ \tilde{T}_1(r) = B_1 K_0(q_1 r) & r \ge r_0. \end{cases} \tag{8}$$

After applying the interface conditions, we have a linear system of equations that can be solved yielding

$$A_0 = \frac{-\tilde{P}_0}{\pi r_0^2 L \kappa_0 q_0^2}\left[\frac{1}{\kappa_0 q_0 I_1(q_0 r_0)\left(\frac{1}{\kappa_1 q_1}\frac{K_0(q_1 r_0)}{K_1(q_1 r_0)} + \mathcal{R}_{0,1}\right) + I_0(q_0 r_0)}\right], \tag{9a}$$

$$B_1 = \frac{\tilde{P}_0}{\pi r_0^2 L \kappa_0 q_0^2}\left[\frac{1}{\kappa_1 q_1 K_1(q_1 r_0)\left(\frac{1}{\kappa_0 q_0}\frac{I_0(q_0 r_0)}{I_1(q_0 r_0)} + \mathcal{R}_{0,1}\right) + K_0(q_1 r_0)}\right], \tag{9b}$$

$$A_1 = B_0 = 0. \tag{9c}$$

The average temperature oscillation of the wire is then

$$\tilde{T}_{2\omega,avg} = \frac{1}{r_0}\int_0^{r_0} \tilde{T}_0(r)dr = \frac{1}{r_0}\int_0^{r_0} A_0 I_0(q_0 r)dr + \frac{\tilde{P}_0}{\pi r_0^2 L \kappa_0 q_0^2}. \tag{10}$$

The integration of $I_0(q_0 r)$ over the wire radius can be expressed as a series expansion for small values of $r$ [which in our case is $\mathcal{O}(10^{-6})$] and dropping all but the lowest order term,

$$\int_0^{r_0} A_0 I_0(q_0 r)dr \approx A_0\left[r + \frac{q_0^2 r^3}{12} + \frac{q_0^4 r^5}{320} + \mathcal{O}\left(r^7\right)\right]_0^{r_0} \approx A_0 r_0. \tag{11}$$

The rms temperature oscillation of the infinitely long hot-wire at $2\omega$ is then

$$\tilde{T}_{2\omega,avg} \cong \frac{\tilde{P}_0}{\pi r_0^2 L \kappa_0 q_0^2} \times \left[1 - \frac{1}{\kappa_0 q_0 I_1(q_0 r_0)\left(\frac{1}{\kappa_1 q_1}\frac{K_0(q_1 r_0)}{K_1(q_1 r_0)} + \mathcal{R}_{0,1}\right) + I_0(q_0 r_0)}\right]. \tag{12}$$

If the same simplifying assumptions from transient hot-wire are used (negligible wire heat capacity), Eq. (12) reduces to the line-source solution form

$$\tilde{T}_{2\omega,line} \cong \frac{\tilde{P}_0}{2\pi r_0 L}\left[\frac{1}{\kappa_1 q_1}\frac{K_0(q_1 r_0)}{K_1(q_1 r_0)} + \mathcal{R}_{0,1}\right]. \tag{13}$$

Equations (12) and (13) converge for low frequencies that satisfy the condition

$$\omega \ll \left(\frac{4}{\pi r_0^2}\right)\left(\frac{\kappa_1}{\rho_0 C_0}\right). \tag{14}$$

While it is tempting to use the line-source solution, in practical terms, this requires measurements to be performed at very low frequencies or for very small diameter heating wires to be used. The low frequencies necessary for Eq. (13) when using heating wire diameters of ~10 $\mu$m would require very long measurement times (possibly hours to days),[45] far too long for useful measurements. On the other hand, practical measurement frequency ranges can be attained if heating wire diameters are on the scale of ~10 to 100 nm. Such small diameters, however, lead to very delicate devices that may have difficulty operating in harsh or corrosive chemical environments inherent to many materials of interest.

The line-source solution [Eq. (13)] was initially proposed to analyze early frequency dependent hot-wire experiments due to a desired simple analysis and assumption that the simplifications used in time-domain hot-wire could also apply.[56,57] More recently, the infinite length solution [Eq. (12)] has been used for the majority of data fitting in the literature; however, there are often deviations from the experimental results at lower frequencies.[45] Line-source and infinite length hot-wire solution curves are shown in Fig. 3 compared to experimental results for a hot-wire in argon atmosphere. This clearly shows the deviation between the experiment and the infinitely long wire model at low frequencies, which is particularly pronounced in the out-of-phase component [$Y$, $\text{Im}\left(\tilde{T}_{2\omega,avg}\right)$] of the solution compared to the in-phase component [$X$, $\text{Re}\left(\tilde{T}_{2\omega,avg}\right)$], and it is due to the finite length of the suspended heating wires used in the experiments. The line-source solution, however, never approaches the experimental results since it does not include the strong damping effect of the wire heat capacity. In Sec. III B, we detail an analytical solution that accounts for this finite length in the thermal model.

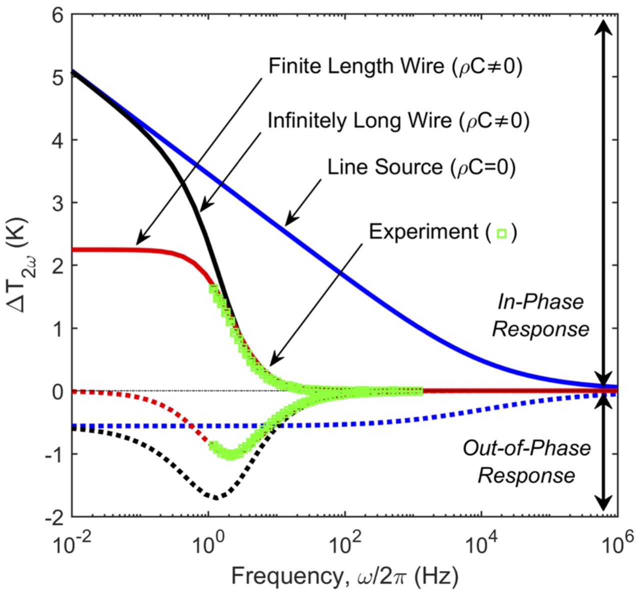

**FIG. 3**. Various modeled (solid and dashed lines) vs experimental (green squares) frequency-dependent temperature rise for a hot-wire sensor (6 mm long, 25 $\mu$m diameter Pt wire) in argon. Modeled solutions used hot-wire geometry and thermal properties of argon as inputs with no fitting. Modeled and experimental in-phase [$X$, Re$(\tilde{T}_{2\omega,avg})$] and out-of-phase [$Y$, Im$(\tilde{T}_{2\omega,avg})$] temperature components are shown with the finite length wire solution showing the best agreement with the experimental results.

## B. Case 2: Including axial conduction (finite length wire)

In any real hot-wire experiment, the wire will be of finite length, and in some experimental situations, short length wires are necessary due to the small volumes of sample materials available. The geometry and boundary conditions of case 2 are shown in Fig. 2(b) but with no coating thickness, $d = 0$. Note the assumption that the temperature rise at the ends of the wire is negligible and valid for all cases in this work where the conductance to the substrate is large compared to that of the wire. The validity of the assumption may need to be re-evaluated in cases when thermal conductivity of the sample is comparable to that of the substrate, which could occur in molten metal samples.

Any solution to the heat equation in this case is complicated by the fact that we must solve a partial differential equation in a two-dimensional (2-D) cylindrical coordinate system. To simplify and analytically solve Eq. (3), we can separate the temperature function, $\tilde{T}_N(r,z)$, into radial, $r$, and axial, $z$, components via a finite Fourier transform due to the finite region over which the $z$-dimension is considered. Here, the transformed temperature, $\tau_N$, is

$$\tau_N(n,r) = \int_0^l K_e(n,z)\tilde{T}_N(r,z)dz, \tag{15}$$

where the inverse transform is

$$\tilde{T}_N(r,z) = \sum_{n=1}^{\infty} K_e(n,z)\tau_N(n,r). \tag{16}$$

The kernel function[58] for the Dirichlet-type axial boundary conditions specified in Eq. (4) is

$$K_e(n,z) = \sqrt{\frac{2}{l}}\sin(\lambda_n z), \tag{17}$$

and the $z$-dimension Fourier transform variable is

$$\lambda_n = \frac{\pi(2n-1)}{2l}, \tag{18}$$

where $n = 1, 2, 3$, etc. The transformed heat equation, now depending on only the radial dimension, is

$$\frac{\partial^2\tau_N}{\partial r^2} + \frac{1}{r}\frac{\partial\tau_N}{\partial r} - \varphi_N^2\tau_N + \sqrt{\frac{2}{l}}\left(\frac{\tilde{P}_N'''}{\kappa_N\lambda_n}\right) = 0, \tag{19}$$

where

$$\varphi_N = \sqrt{\lambda_n^2 + \frac{i2\omega\rho_N C_N}{\kappa_N}} = \sqrt{\lambda_n^2 + q_N^2}, \tag{20}$$

and the solution to Eq. (18) is

$$\tau_N(n,r) = A_N' I_0(\varphi_N r) + B_N' K_0(\varphi_N r) + \sqrt{\frac{2}{l}}\left(\frac{\tilde{P}_N'''}{\kappa_N\lambda_n\varphi_N^2}\right). \tag{21}$$

The wave-vector in this case, $\varphi_N$, is more complicated than that of case 1 and has both radial thermal wave-vector, $q_N$, and axial spatial wave-vector, $\lambda_n$, components.

After transforming and applying the radial boundary conditions from Eq. (4), the transformed temperature distributions for the wire and sample volumes are

$$\tau_N(n,r) = \begin{cases} \tau_0(n,r) = A_0' I_0(\varphi_0 r) + \sqrt{\frac{2}{l}}\left(\frac{\tilde{P}_0}{\pi r_0^2 L\kappa_0\lambda_n\varphi_0^2}\right) & 0 \le r \le r_0 \\ \tau_1(n,r) = B_1' K_0(\varphi_1 r) & r \ge r_0. \end{cases} \tag{22}$$

At each layer interface, the same previous heat flux and temperature continuity conditions must hold [Eq. (5)], which results in a linear system of equations that can be solved to yield

$$A_0' = -\sqrt{\frac{2}{l}}\left(\frac{\tilde{P}_0}{\pi r_0^2 L\kappa_0\lambda_n\varphi_0^2}\right) \times \left[\frac{1}{\kappa_0\varphi_0 I_1(\varphi_0 r_0)\left(\frac{1}{\kappa_1\varphi_1}\frac{K_0(\varphi_1 r_0)}{K_1(\varphi_1 r_0)} + \mathcal{R}_{0,1}\right) + I_0(\varphi_0 r_0)}\right], \tag{23a}$$

$$B_1' = \sqrt{\frac{2}{l}}\left(\frac{\tilde{P}_0}{\pi r_0^2 L\kappa_0\lambda_n\varphi_0^2}\right) \times \left[\frac{1}{\kappa_1\varphi_1 K_1(\varphi_1 r_0)\left(\frac{1}{\kappa_0\varphi_0}\frac{I_0(\varphi_0 r_0)}{I_1(\varphi_0 r_0)} + \mathcal{R}_{0,1}\right) + K_0(\varphi_1 r_0)}\right], \tag{23b}$$

$$A_1' = B_0' = 0. \tag{23c}$$

The steady-state temperature oscillations can then be recovered using the inverse transform [Eq. (16)].

To find the average temperature rise of the hot-wire, which is the quantity measured via the voltage difference across the suspended wire length, we apply the reverse transform to recover $\tilde{T}_0(r,z)$ and average over the length and radius of the wire element,

$$\begin{aligned}\tilde{T}_{2\omega,avg} &= \frac{1}{r_0}\int_0^{r_0}\frac{1}{l}\int_0^{l}\tilde{T}_0(r,z)dzdr\\ &= \frac{1}{r_0}\int_0^{r_0}\frac{1}{l}\int_0^{l}\sum_{n=1}^{\infty}K_e(n,z)\cdot\tau_0(n,r)dzdr\\ &= \sum_{n=1}^{\infty}\left[\frac{1}{l}\int_0^{l}K_e(n,z)dz\right]\left[\frac{1}{r_0}\int_0^{r_0}A'_0I_0(\varphi_0 r)dr\right.\\ &\quad\left.+\sqrt{\frac{2}{l}}\left(\frac{\tilde{P}_0}{\pi r_0^2 L\kappa_0\lambda_n\varphi_0^2}\right)\right].\end{aligned}\tag{24}$$

Integrating the kernel function over the wire half-length, $l$, leads to

$$\int_0^{l}K_e(n,z)dz=\int_0^{l}\sqrt{\frac{2}{l}}\sin(\lambda_n z)dz=\sqrt{\frac{2}{l}}\left(\frac{1}{\lambda_n}\right),\tag{25}$$

and integration of $I_0(\varphi_0 r)$ over the wire radius can be approximated, as in Eq. (11). The average measured rms temperature of the modularly heated finite-length wire is

$$\begin{aligned}\tilde{T}_{2\omega,avg} &\cong \sum_{n=1}^{\infty}\frac{8\tilde{P}_0}{\pi r_0^2 L^3\kappa_0\lambda_n^2\varphi_0^2}\\ &\quad\times\left[1-\frac{1}{\kappa_0\varphi_0 I_1(\varphi_0 r_0)\left(\frac{1}{\kappa_1\varphi_1}\frac{K_0(\varphi_1 r_0)}{K_1(\varphi_1 r_0)}+\mathcal{R}_{0,1}\right)+I_0(\varphi_0 r_0)}\right].\end{aligned}\tag{26}$$

At first glance, this solution appears similar in form to that of the infinite length hot-wire considered in case 1 [Eq. (12)]. Closer inspection, however, shows that the spatial wave-vector, $\lambda_n$, significantly modifies the finite length wire temperature rise at lower frequencies, as observed in Fig. 3. Since $q_N \propto \omega$, the temperature rise is still dampened as the frequency increases due to shortening of the thermal penetration depth. Meanwhile, $\lambda_n \propto L^{-1}$ induces an upper limit to the temperature rise even as $\omega$ decreases because the thermal penetration depth becomes limited by the length of the wire itself (terminating at the thermal reservoirs at the wire endpoints). This behavior very accurately captures the shape of the argon experimental data (experiment in Fig. 3), and in particular, the out-of-phase $[Y, \mathrm{Im}(\tilde{T}_{2\omega,avg})]$ component of the model very accurately matches the experimental data. Of important note is how close the in-phase $[X, \mathrm{Re}(\tilde{T}_{2\omega,avg})]$ curves for the infinite and finite length solutions [Eqs. (12) and (26), respectively] are to one another above 1 Hz. For this reason, it is important to use out-of-phase experimental data to fit to the thermal model or else incorrect thermal properties may be calculated.

### C. Case 3: Finite length hot-wire with insulating coating (3-layer)

For the last case, we solve for the temperature distribution within a suspended cylindrical wire of radius $r_0$ and length $L = 2l$ with an electrically insulating coating of thickness $d = r_1 - r_0$ and surrounded by a semi-infinite thermally conductivity medium that extends very far away from the wire ($r \to \infty$). This system is composed of three layers: the wire ($N = 0$), the coating ($N = 1$), and the surrounding sample ($N = 2$), shown in Fig. 2(b). Applying boundary conditions from case 2 results in

$$\tau_N(n,r)=\begin{cases}\tau_0(n,r)=A_{c,0}I_0(\varphi_0 r)+\sqrt{\frac{2}{l}}\left(\frac{\tilde{P}_0}{\pi r_0^2 L\kappa_0\lambda_n\varphi_0^2}\right) & 0\le r\le r_0\\ \tau_1(n,r)=A_{c,1}I_0(\varphi_1 r)+B_{c,1}K_0(\varphi_1 r) & r_0\le r\le r_1\\ \tau_2(n,r)=B_{c,2}K_0(\varphi_2 r) & r\ge r_1.\end{cases}\tag{27}$$

At each layer interface, heat flux and temperature continuity conditions must hold and include possible wire-coating and coating-sample interfacial thermal resistances, $\mathcal{R}_{0,1}$ and $\mathcal{R}_{1,2}$, respectively. This results in a linear system of equations that can be solved to find

$$\begin{aligned}A_{c,0} &= \sqrt{\frac{2}{l}}\left(\frac{\tilde{P}_0}{\pi r_0^2 L\kappa_0\lambda_n\varphi_0^2}\right)\left(\frac{\kappa_1\varphi_1}{\kappa_0\varphi_0}\right)\left(\frac{1}{\alpha\delta-\gamma\beta}\right)\\ &\quad\times\left[\frac{\beta I_1(\varphi_1 r_0)-\alpha K_1(\varphi_1 r_0)}{I_1(\varphi_0 r_0)}\right],\end{aligned}\tag{28a}$$

$$A_{c,1}=\sqrt{\frac{2}{l}}\left(\frac{\tilde{P}_0}{\pi r_0^2 L\kappa_0\lambda_n\varphi_0^2}\right)\left(\frac{\beta}{\alpha\delta-\gamma\beta}\right),\tag{28b}$$

$$B_{c,1}=\sqrt{\frac{2}{l}}\left(\frac{\tilde{P}_0}{\pi r_0^2 L\kappa_0\lambda_n\varphi_0^2}\right)\left(\frac{\alpha}{\alpha\delta-\gamma\beta}\right),\tag{28c}$$

$$\begin{aligned}B_{c,2} &= -\sqrt{\frac{2}{l}}\left(\frac{\tilde{P}_0}{\pi r_0^2 L\kappa_0\lambda_n\varphi_0^2}\right)\left(\frac{\kappa_1\varphi_1}{\kappa_0\varphi_0}\right)\left(\frac{1}{\alpha\delta-\gamma\beta}\right)\\ &\quad\times\left[\frac{\beta I_1(\varphi_1 r_1)-\alpha K_1(\varphi_1 r_1)}{K_1(\varphi_2 r_1)}\right],\end{aligned}\tag{28d}$$

where

$$\alpha=\kappa_1\varphi_1 I_1(\varphi_1 r_1)\left(\frac{1}{\kappa_2\varphi_2}\frac{K_0(\varphi_2 r_1)}{K_1(\varphi_2 r_1)}+\mathcal{R}_{1,2}\right)+I_0(\varphi_1 r_1),\tag{29a}$$

$$\beta=\kappa_1\varphi_1 K_1(\varphi_1 r_1)\left(\frac{1}{\kappa_2\varphi_2}\frac{K_0(\varphi_2 r_1)}{K_1(\varphi_2 r_1)}+\mathcal{R}_{1,2}\right)-K_0(\varphi_1 r_1),\tag{29b}$$

$$\delta=\kappa_1\varphi_1 K_1(\varphi_1 r_0)\left(\frac{1}{\kappa_0\varphi_0}\frac{I_0(\varphi_0 r_0)}{I_1(\varphi_0 r_0)}+\mathcal{R}_{0,1}\right)+K_0(\varphi_1 r_0),\tag{29c}$$

$$\gamma=\kappa_1\varphi_1 I_1(\varphi_1 r_0)\left(\frac{1}{\kappa_0\varphi_0}\frac{I_0(\varphi_0 r_0)}{I_1(\varphi_0 r_0)}+\mathcal{R}_{0,1}\right)-I_0(\varphi_1 r_0).\tag{29d}$$

The steady-state temperature oscillations can then be found using the inverse transform [Eq. (16)]. To find the average temperature of the wire, which is what is measured using the voltage difference across the wire length, we integrate over the length and radius, as in Eqs. (11), (24), and (25). The average measured temperature of the modularly heated wire is then

$$\begin{aligned}\tilde{T}_{2\omega,avg} &\cong \sum_{n=1}^{\infty}\frac{8\tilde{P}_0}{\pi r_0^2 L^3\kappa_0\lambda_n^2\varphi_0^2}\left\{1+\left(\frac{\kappa_1\varphi_1}{\kappa_0\varphi_0}\right)\left(\frac{1}{\alpha\delta-\gamma\beta}\right)\right.\\ &\quad\left.\times\left[\frac{\beta I_1(\varphi_1 r_0)-\alpha K_1(\varphi_1 r_0)}{I_1(\varphi_0 r_0)}\right]\right\}.\end{aligned}\tag{30}$$

We can simplify this case by assuming that the coating on the wire acts as a purely thermally resistive element ($d/\kappa_1$), which becomes

$$\tilde{T}_{2\omega,avg} \cong \sum_{n=1}^{\infty} \frac{8\tilde{P}_0}{\pi r_0^2 L^3 \kappa_0 \lambda_n^2 \varphi_0^2} \times \left[1 - \frac{1}{\kappa_0\varphi_0 I_1(\varphi_0 r_0)\left(\frac{1}{\kappa_2\varphi_2}\frac{K_0(\varphi_2 r_0)}{K_1(\varphi_2 r_0)} + \mathcal{R}_{0,1} + \frac{d}{\kappa_1} + \mathcal{R}_{1,2}\right) + I_0(\varphi_0 r_0)}\right] \qquad (31)$$

and closely resembles the case 2 solution [Eq. (26)] but includes additional thermal resistance terms, $d/\kappa_1$ and $\mathcal{R}_{1,2}$. The $\varphi_2$ term in Eq. (31) is equivalent to $\varphi_1$ in Eq. (26), both representing the thermal properties of the sample volume.

## IV. MODEL COMPARISON

The solutions for cases 1, 2, and 3 add increasing complexity as more details are considered but allow the models to more accurately capture the physical behavior of the experiment. Importantly, this also exposes how simplifying assumptions and neglecting certain terms can lead to deviations in the models from reality. Most significant are assuming infinite length (case 1 vs case 2, shown in Fig. 4), neglecting a coating layer (case 2 vs case 3, shown in Fig. 5), and neglecting the interfacial thermal resistance [assuming $\mathcal{R}_{0,1}$ in Eq. (26) of case 2 is negligible, shown in Fig. 6]. For each comparison, we can see the frequency-dependent temperature rise deviation in the in-phase and out-of-phase solution components when considering three different material cases: gas ($\kappa = 0.01$ W m$^{-1}$ K$^{-1}$ and $\rho C = 1 \times 10^3$ J m$^{-3}$ K$^{-1}$), liquid ($\kappa = 0.1$ W m$^{-1}$ K$^{-1}$ and $\rho C = 3 \times 10^6$ J m$^{-3}$ K$^{-1}$), and low thermal conductivity solid ($\kappa = 1$ W m$^{-1}$ K$^{-1}$, $\rho C = 3 \times 10^6$ J m$^{-3}$ K$^{-1}$).

Making the infinite length approximation is very attractive for hot-wire setups where the aspect ratio of the wire, $r_0/L$, is very small. This would lead to $\varphi_N \to q_N$ in Eq. (26) and $\sum_{n=1}^{\infty} 8(L\lambda_n\varphi_0)^{-2} \to 8(\pi q_0)^{-2}\sum_{n=1}^{\infty}(2n-1)^{-2} = (q_0)^{-2}$, which results in Eq. (26) converging to Eq. (12). However, as seen in the literature,[45] this assumption may not be valid over the entire observed frequency range. In Fig. 4, we show the deviation in the temperature rise calculated using Eqs. (12) and (26) as a function of hot-wire length for the 1–1000 Hz frequency range considered in this study (using a 25 $\mu$m diameter Pt wire). As the thermal conductivity of the sample increases, shorter length wires exhibit less deviation from the infinite length solution due to the larger heat conduction from the wire surface compared to axial conduction. However, to achieve a temperature deviation less than 1% across the entire frequency spectrum, the wire needs to be longer than 100 mm. Interestingly, we observe that the in-phase deviation exhibits a locus frequency for which the deviation is zero and is positive for lower frequencies and negative for those higher. The out-of-phase deviation on the other-hand is positive over the entire frequency range and monotonically decreases with an increase in frequency.

When considering a coating layer, the deviation between Eq. (26) (no coating) and (30) (with coating) is shown in Fig. 5, assuming 5 mm wire length. In this case, we assume the coating is an

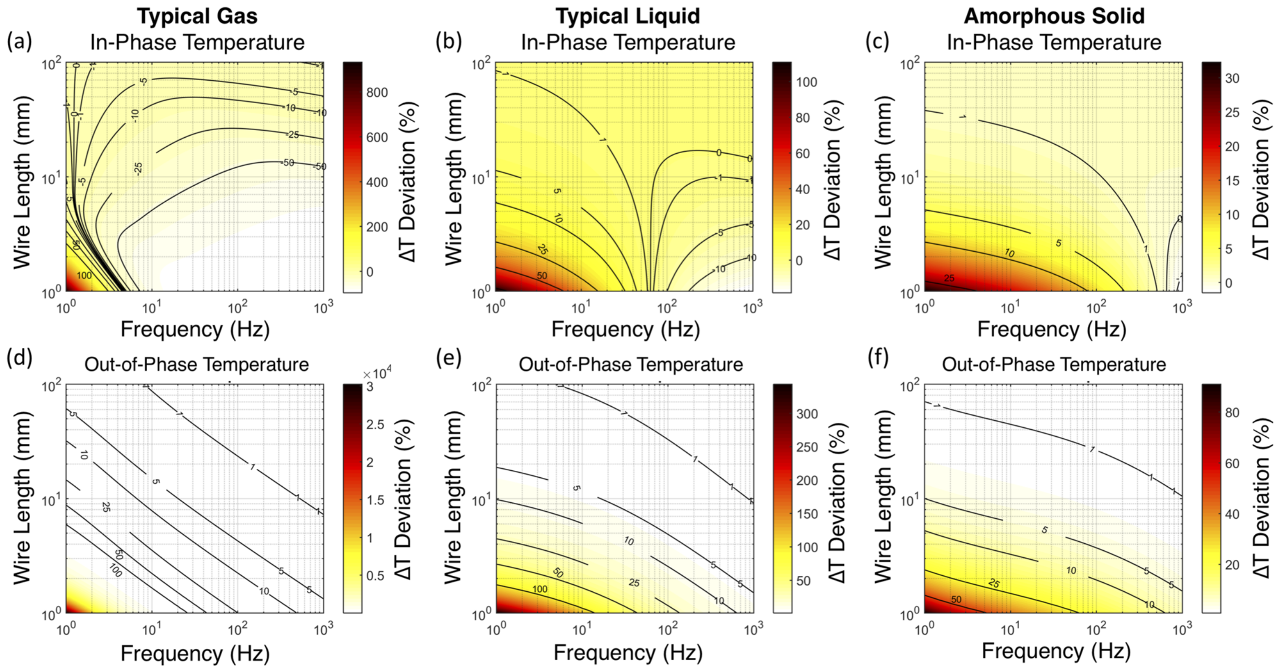

**FIG. 4**. Deviation in in-phase and out-of-phase temperature rise from using the infinite length model [Eq. (12)] as opposed to the finite length model [Eq. (26)] for [(a) and (d)] a typical gas ($\kappa = 0.01$ W m$^{-1}$ K$^{-1}$ and $\rho C = 1 \times 10^3$ J m$^{-3}$ K$^{-1}$), [(b) and (e)] liquid/polymer ($\kappa = 0.1$ W m$^{-1}$ K$^{-1}$ and $\rho C = 3 \times 10^6$ J m$^{-3}$ K$^{-1}$), and [(c) and (f)] low thermal conductivity amorphous solid ($\kappa = 1$ W m$^{-1}$ K$^{-1}$ and $\rho C = 3 \times 10^6$ J m$^{-3}$ K$^{-1}$).

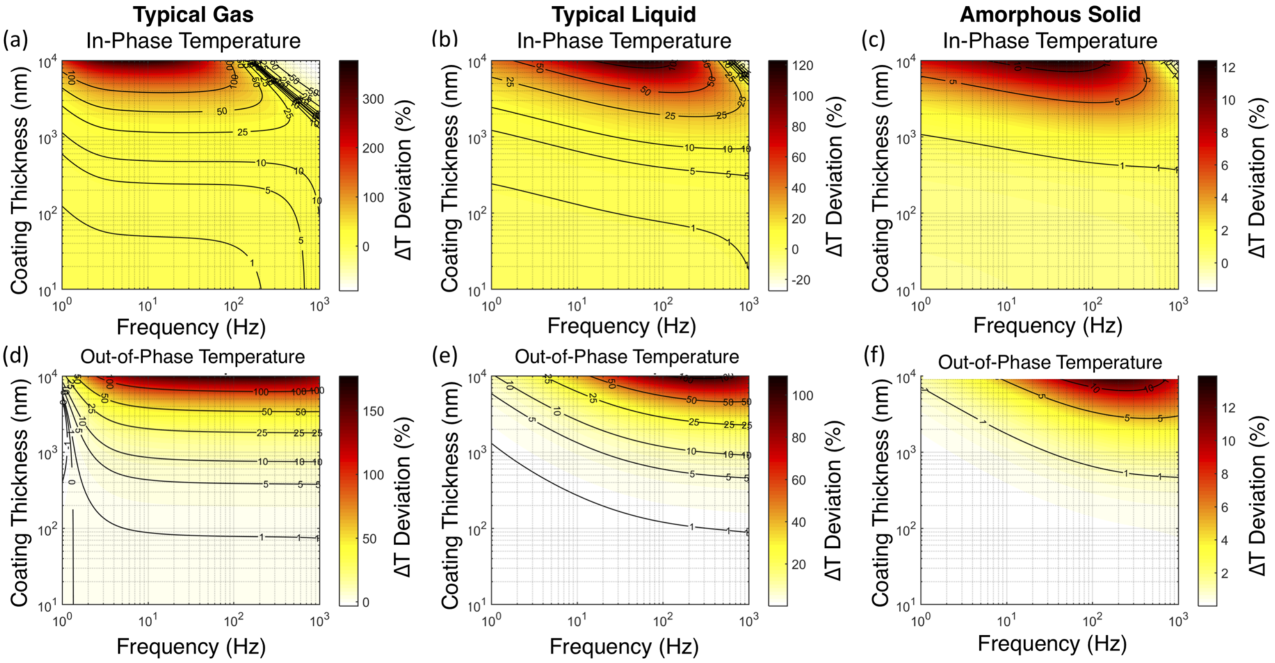

**FIG. 5**. Deviation in in-phase and out-of-phase temperature rise from neglecting coating thermal effects in Eq. (30) for [(a) and (d)] a typical gas ($\kappa = 0.01$ W m$^{-1}$ K$^{-1}$ and $\rho C = 1 \times 10^3$ J m$^{-3}$ K$^{-1}$), [(b) and (e)] liquid/polymer ($\kappa = 0.1$ W m$^{-1}$ K$^{-1}$ and $\rho C = 3 \times 10^6$ J m$^{-3}$ K$^{-1}$), and [(c) and (f)] low thermal conductivity solid ($\kappa = 1$ W m$^{-1}$ K$^{-1}$ and $\rho C = 3 \times 10^6$ J m$^{-3}$ K$^{-1}$).

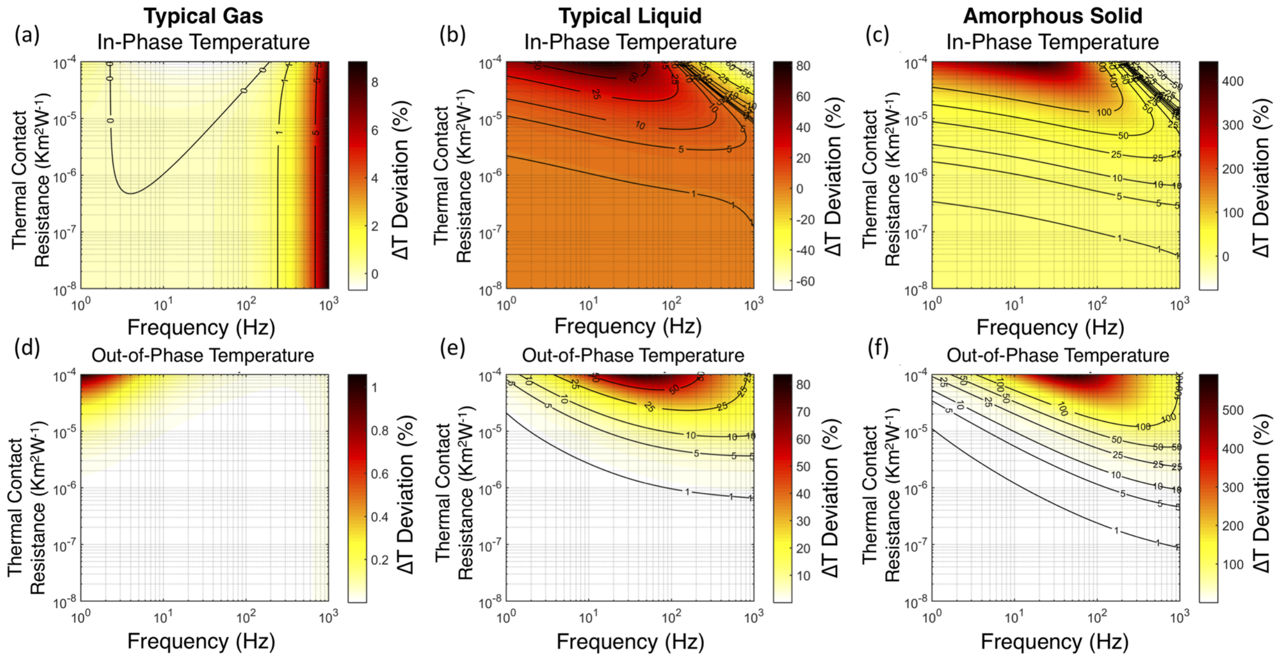

**FIG. 6**. Deviation in in-phase and out-of-phase temperature rise from neglecting the thermal contact resistance in Eq. (26) for [(a) and (d)] a typical gas ($\kappa = 0.01$ W m$^{-1}$ K$^{-1}$ and $\rho C = 1 \times 10^3$ J m$^{-3}$ K$^{-1}$), [(b) and (e)] liquid/polymer ($\kappa = 0.1$ W m$^{-1}$ K$^{-1}$ and $\rho C = 3 \times 10^6$ J m$^{-3}$ K$^{-1}$), and [(c) and (f)] low thermal conductivity solid ($\kappa = 1$ W m$^{-1}$ K$^{-1}$ and $\rho C = 3 \times 10^6$ J m$^{-3}$ K$^{-1}$).

amorphous alumina[59] with thermal properties of $\kappa = 1$ W m$^{-1}$ K$^{-1}$ and $\rho C = 2.3 \times 10^6$ J m$^{-3}$ K$^{-1}$. Here, we see that as sample thermal conductivity increases, approaching that of the coating, the temperature deviation decreases over the entire frequency range. For very thick coatings, greater than several micrometers, the deviation increases for all cases. For experimental setups which include a protective or insulating coating, it is advisable to take the effects of the coating into account and use Eq. (30) over Eq. (26) for coatings thicker than 100 nm. This may differ for other coating materials, for example, the most likely alternative to an oxide-based coating is a polymer based one, which will have a larger temperature deviation due to the expected thicker layer and lower thermal conductivity (~0.1–0.2 W m$^{-1}$ K$^{-1}$), making it even more important to include the coating in the analysis model.

Finally, we investigate the effects of interfacial thermal resistance, $\mathcal{R}_{0,1}$, in Eq. (26), not considering a coating on the wire for simplicity (again assuming 5 mm wire length). Figure 6 shows that the temperature deviation when including interfacial thermal resistance increases, expectedly, as the thermal resistance increases. Furthermore, the deviation increases as the sample thermal conductivity increases because the effective thermal resistance of the sample decreases.

## V. FITTING ERROR

In Sec. IV, we demonstrated the effects of ignoring parameters and simplifying assumptions over the full heating frequency spectrum. In this section, we focus on the effects of fitting the models to the experimental data. To investigate this, we checked how making the previous simplifications would affect fitting the thermal conductivity of the sample to the un-simplified cases, shown in Fig. 7. We fit over the entire 1–1000 Hz frequency range for the three sample thermal property situations listed previously and calculated the error in the fitted thermal conductivity using a least-squares fitting algorithm. Here, we assumed a 25 $\mu$m diameter Pt wire for all cases [and 5 mm wire length when not considering the length dependence in Figs. 7(b) and 7(c)]. A coating is only considered in the case of Fig. 7(b).

As expected, very long hot-wires should be used if the temperature rise data are fit using the infinite length model [Eq. (12)]. This is particularly important for low thermal conductivity samples, such as gases, where more of the generated heat is axially conducted away. To have less than 5% error in the fitted thermal conductivity for this case, the hot-wire should be longer than 100 mm for gas-like materials and >20 mm for liquids and polymers [Fig. 7(a)]. The thermal conductivity error increases significantly if the wire is too short; for example, fitting to Eq. (12) instead of Eq. (26) for measurements in a gas will overpredict the thermal conductivity by more than 100%. This highlights the importance of using the finite length model when using short hot-wires, which is likely the case when measuring small experimental samples. This requires that the hot-wire length, $L$, be well-know, either via direct measurement, the recommended electrical resistance measurement method (discussed above), or calibration in a known material, beforehand.

If the measurement requires a coating on the hot-wire, either for electrical insulation or chemical resistance, it is recommended to use Eq. (30), which considers the coating, over Eq. (26), which neglects the coating. The full three-layer model [Eq. (30)] should be used if the coating is ~1 $\mu$m or thicker to keep fitting errors below 5% [Fig. 7(b)]. In this case, an oxide coating was considered, but the use of a polymeric coating could exacerbate this effect due to its lower intrinsic thermal conductivity and it likely being a rather thick layer.

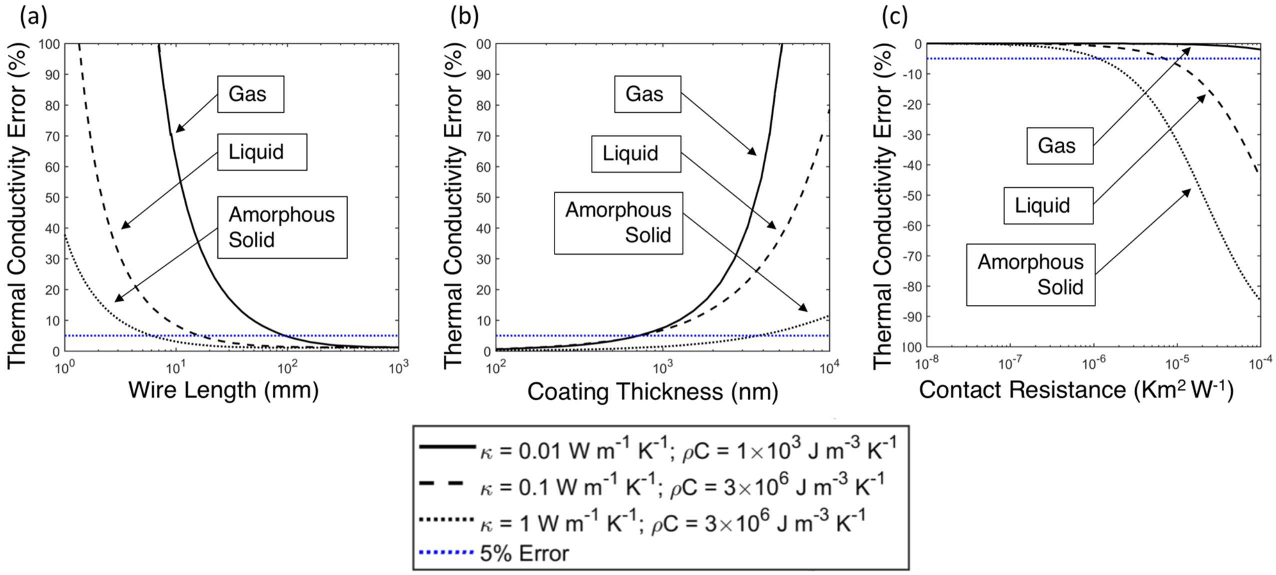

**FIG. 7**. Error in fitted thermal conductivity for a typical gas, liquid/polymer, and low thermal conductivity solid cases when (a) using the infinite length model [Eq. (12)] as opposed to the finite length model [Eq. (26)], (b) neglecting the coating effect in Eq. (30), and (c) neglecting the thermal contact resistance in Eq. (26) or (30). All assume a 25 $\mu$m diameter Pt hot-wire while (b) and (c) also assume a 5 mm long hot-wire.

Whether neglecting the thermal contact resistance between the sample and the hot-wire leads to significant fitting error is a slightly more difficult question due to large variability between different materials. In this case, we check the effect of thermal contact resistances as low as $10^{-8}$ K m$^2$/W and as high as $10^{-4}$ K m$^2$/W [Fig. 7(c)]. In this case, the effect of contact resistance increases as the thermal conductivity of the sample increases. In order to ensure <5% error in the fitted thermal conductivity, the contact resistance should be less than $10^{-6}$ K m$^2$/W. This is particularly fortuitous as this cutoff value is larger than that experimentally measured for many hard–soft interfaces with the majority between $2 \times 10^{-9}$ K m$^2$/W and $3 \times 10^{-7}$ K m$^2$/W,[60] specifically $8 \times 10^{-9}$ K m$^2$/W for the Pt-water interface[61] and between $10^{-7}$ K m$^2$/W and $3 \times 10^{-6}$ K m$^2$/W for the contact between molten metals and a solid surface.[62] Care may be needed for measuring polymer samples, however, which are sometimes reported to be close to the cutoff contact resistance value, $3 \times 10^{-6}$ K m$^2$/W and $2 \times 10^{-5}$ K m$^2$/W, and may increase with ambient temperature and depend on the hot-wire diameter.[63]

## VI. MODEL SENSITIVITY

The finite length model [Eq. (26)] requires either knowledge of the heat capacity, $\rho C$, of the sample or simultaneous fitting of both the thermal conductivity and the heat capacity, $\kappa$ and $\rho C$. Both properties influence the frequency-dependent temperature rise but in different portions of the spectrum. Additionally, Eq. (26) contains both in-phase [$X$, $\mathrm{Re}(\tilde{T}_{2\omega,avg})$] and out-of-phase [$Y$, $\mathrm{Im}(\tilde{T}_{2\omega,avg})$] components, which each contain different information regarding the thermal properties of the sample. The extent to which Eq. (26) is affected by $\kappa$ and $\rho C$ can be examined by studying the sensitivity of the model to each material parameter.[36,42] The sensitivity of the model relates how much the measured temperature rise would change in response to a change in the sample thermal conductivity ($\kappa$) or heat capacity ($\rho C$), via the normalized derivative with respect to thermal conductivity, $(\kappa/T) \cdot \partial T/\partial \kappa$, or heat capacity, $(\rho C/T) \cdot \partial T/\partial \rho C$. Figure 8 shows the in-phase and out-of-phase sensitivities of the hot-wire measurement (using a 5 mm long, 25 $\mu$m diameter Pt wire) to sample $\kappa$ and $\rho C$ over a 1–1000 Hz spectrum for gas-like [Fig. 8(a)], liquid/polymer [Fig. 8(b)], and low thermal conductivity solid [Fig. 8(c)] materials.

For gas-like thermal properties [Fig. 8(a)], the $Y$ component is more sensitive to changes in $\kappa$ than in $\rho C$ at 1 Hz, but the sensitivity of both out-of-phase components quickly drops to zero as the frequency increases. As this occurs, the sensitivity of the $X$ component increases with frequency, quickly plateauing for $\kappa$, while steadily increasing for $\rho C$ but always more sensitive to $\kappa$ over the entire frequency spectrum considered here. For materials with higher thermal conductivity and heat capacity [Figs. 8(b) and 8(c)], the sensitivities follow similar trends but are shifted to higher frequency as $\kappa$ increases. For low frequencies, the $X$ and $Y$ sensitivities to $\kappa$ are greater in magnitude than that for $\rho C$. All sensitivity to $\rho C$ tends to zero as the frequency decreases, leading to maximum sensitivity to $\kappa$. At higher frequencies, the $Y$ sensitivity to $\kappa$ and $\rho C$ converge and tend to zero. This represents the frequency range where the out-of-phase component is sensitive to the effusivity ($e_{th} = \kappa \rho C$) of the material. The $X$ sensitivities, however, decrease much quicker with an increase in frequency, cross one-another, and pass through zero and continue to increase (the sensitivities flip signs, but the magnitude is increasing after it passes though zero).

The sensitivity analysis provides several take-aways: (1) Lower frequencies are always more sensitive to $\kappa$ than $\rho C$ for both $X$ and $Y$. (2) At low frequencies, the ratio of the sensitivity of $\kappa$ to that of $\rho C$, $S_\kappa/S_{\rho C}$, is larger for the out-of-phase components than for the in-phase. (3) As frequency increases, the $Y$ sensitivity becomes

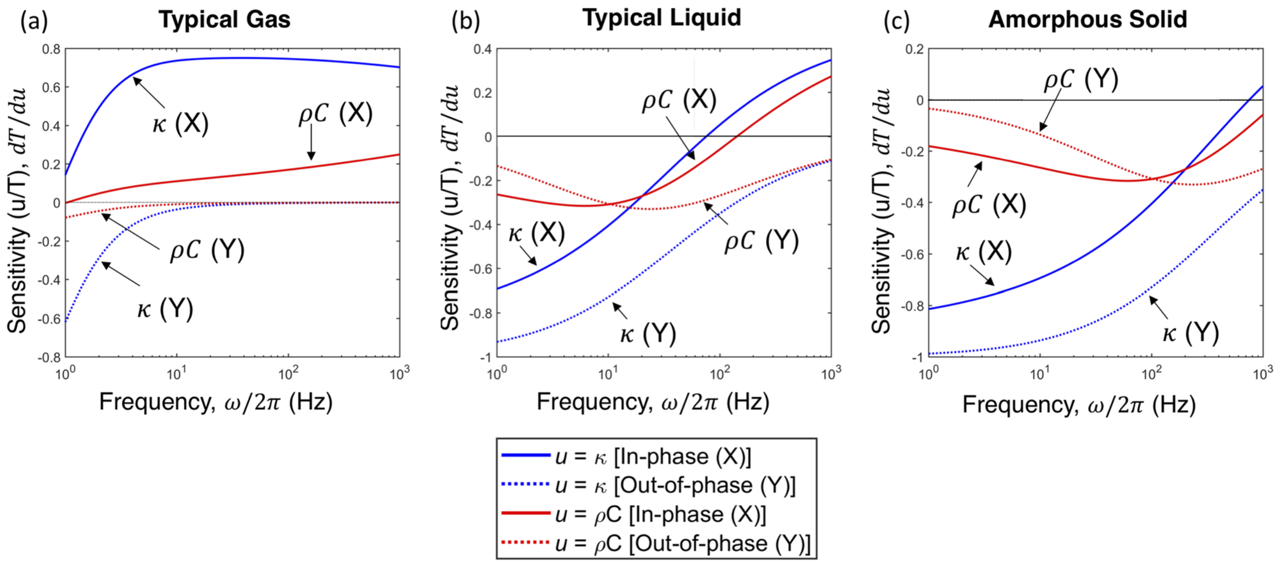

**FIG. 8**. Sensitivity of the in-phase and out-of-phase components of the finite hot-wire length model [Eq. (26)], to thermal conductivity, $\kappa$, and heat capacity, $\rho C$, for (a) typical gas, (b) liquid/polymer, and (c) low thermal conductivity solid. All assume a 5 mm long, 25 $\mu$m diameter Pt hot-wire.

sensitive only to the effusivity of the material. Therefore, when taking and fitting the data for the thermal conductivity, the low frequencies have the largest influence and performing measurements in this range should be prioritized. However, at frequencies below 1 Hz, the increasing thermal penetration depth can grow to include the effects of natural convection (the onset of which can be determined from the Rayleigh number and is dependent on the material tested), leading to errors in fitted thermal conductivity.

## VII. MEASUREMENTS

The designed and fabricated frequency-domain hot-wire chips [chip shown in Fig. 1(b)] were tested in gas (argon[64]) and liquid environments (silicone oil,[65] ethanol,[66–68] methanol,[66] and deionized water[69–71]) with known thermal conductivity to check sensor operation and data analysis. Each test was performed at room temperature (25 °C) over a frequency range of 1–1000 Hz with a heating current of 100 mA (30 mA was used for argon to limit the temperature rise). The Pt hot-wire used for measurements had diameters measured to be 26 $\mu$m, while the wire lengths varied slightly from device to device but were calculated on average to be ∼6.5 ± 1 mm from the measured room temperature electrical resistance (∼1.25 Ω) and resistivity of the wire (0.192 Ω/mm). The Pt wire's thermal conductivity,[72] density,[73] and heat capacity[74] are taken from the literature. As a check, our Pt wire thermal conductivity was calculated using the Wiedemann–Franz ratio and found to be in good agreement with the literature.

The in-phase and out-of-phase experimental data for each test are shown in Fig. 9 along with the least-squares fits using Eq. (30) (where $r_0 = r_1$ because no coating was present on the hot-wires). Fits used Eq. (30) to simultaneously fit both the in-phase ($X$) and out-of-phase ($Y$) data. These fits match the experiments well over the full frequency range measured here, and the resulting fitted thermal conductivities (including fitting error) are shown in each data plot along with the input heat capacity. Of note is that the temperature rise, $\Delta T_{2\omega}$, rapidly attenuates for the gas compared to the liquids. In addition, the low frequency temperature rise of each liquid is inversely proportional to its thermal conductivity. Here, we can also see that the probed volumes, where the volume radius is the thermal penetration depth $[\sqrt{\kappa/(2\omega\rho C)}]$, are rather small at ∼50 $\mu$m to 100 $\mu$m. Not only does this prevent the onset of natural convection (depending on the temperature rise and sample properties) but

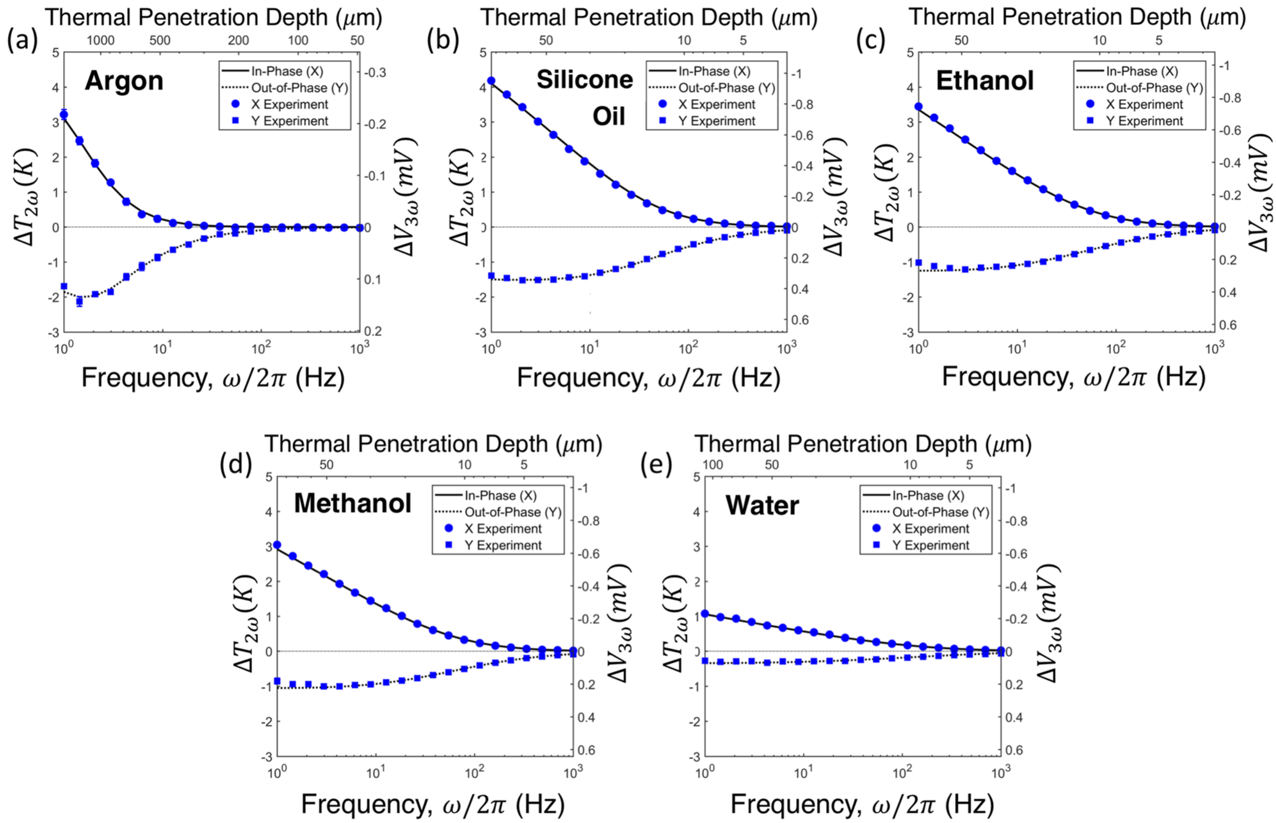

**FIG. 9**. Frequency-domain measurements on reference gas and liquids at 25 °C. Measured thermal conductivity and propagated error using literature values for density and heat capacity: (a) argon gas ($\kappa$ = 0.0207 ± 0.000 79 W m$^{-1}$ K$^{-1}$ and $\rho C$ = 699 J m$^{-3}$ K$^{-1}$), (b) silicone oil ($\kappa$ = 0.143 ± 0.0065 W m$^{-1}$ K$^{-1}$ and $\rho C$ = 1.26 × 10$^{6}$ J m$^{-3}$ K$^{-1}$), (c) ethanol ($\kappa$ = 0.166 ± 0.000 71 W m$^{-1}$ K$^{-1}$ and $\rho C$ = 1.94 × 10$^{6}$ J m$^{-3}$ K$^{-1}$), (d) methanol ($\kappa$ = 0.199 ± 0.000 86 W m$^{-1}$ K$^{-1}$ and $\rho C$ = 2 × 10$^{6}$ J m$^{-3}$ K$^{-1}$), and (e) water ($\kappa$ = 0.63 ± 0.027 W m$^{-1}$ K$^{-1}$ and $\rho C$ = 4.18 × 10$^{6}$ J m$^{-3}$ K$^{-1}$).

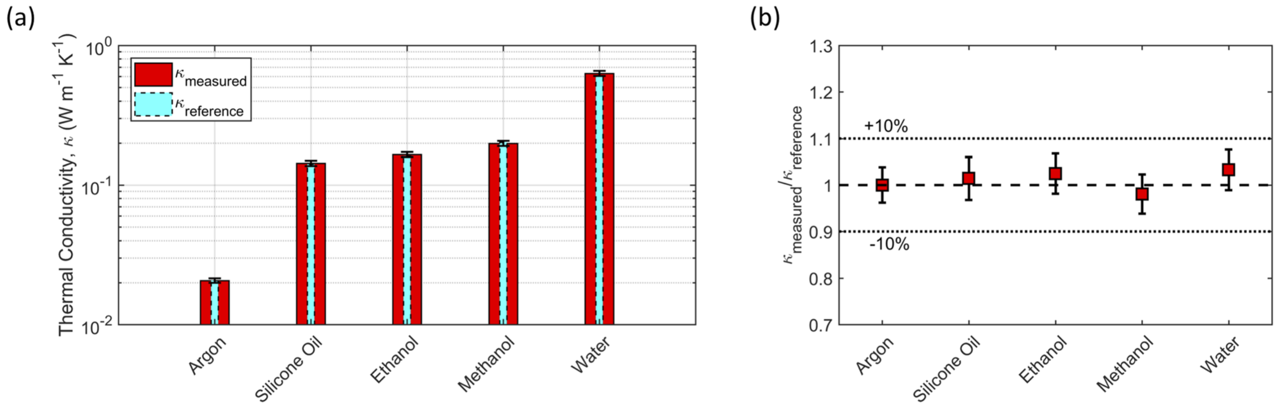

**FIG. 10**. Comparison between the fitted thermal conductivities for the reference gas and liquids and literature values in terms of (a) absolute values and (b) ratios.

is ideal for measuring small batches of material developed in the laboratory to quickly screen compounds without needing to produce large quantities of the material. The fitted $\kappa$ values for each material in comparison to their reference values are shown Fig. 10(a) and exhibit good agreement, being within less than ±10% of the reference [Fig. 10(b)].

The error in the fitted thermal conductivity was calculated both from fits to data including experimental standard deviation from over 50 data points collected at each frequency point and from propagation of error from the measured constants in the model. These include uncertainties in the reference heat capacity (5%), measured radius (1%), coating thickness (5%, if applicable), wire length (2%), and the thermal conductivity (5%) and heat capacity (5%) of the Pt wire itself. To investigate how the error propagates through the model, we checked the proportion each quantity, $\delta\kappa_x$, contributes to the total propagated error, $\delta\kappa_{total}$ (assuming that the error in each term is 10%). The contribution of each uncertainty to the total propagated error for different materials is shown in Fig. 11. For argon and any material with gas-like thermal properties, the error is dominated by uncertainty in the wire radius, $\delta\kappa_{r0}$, and to a lesser extent, the wire length, $\delta\kappa_L$. This relation inverts for the higher thermal conductivity materials, with uncertainty in the length dominating the radius secondary. As the sample thermal conductivity increases, the difference becomes even larger, and one would expect the length uncertainty to become the dominant error source for very high thermal conductivity materials such as liquid metals.

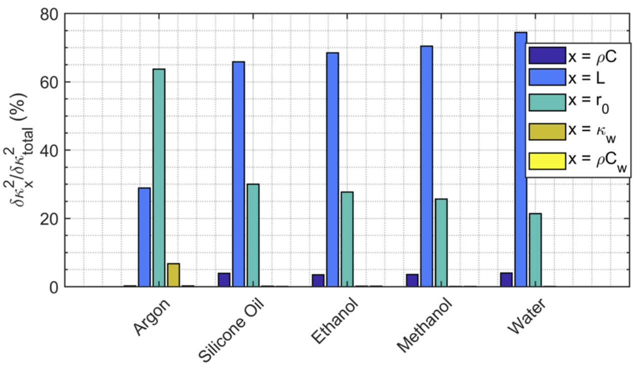

**FIG. 11**. Ratios of the individual uncertainties ($\delta\kappa_x$) in dimensions and material properties to the total propagated measurement uncertainty ($\delta\kappa_{total}$) for the measurements on the reference gas and liquids (assuming equal uncertainty of 10% for each property).

Temperature dependent testing was also performed with an $Al_2O_3$ coated (~250 nm thick) sensor in solid and molten sulfur from 25 °C to 400 °C with measurements taken at approximately every 25 °C. Sulfur was chosen as it is a relatively reactive element with a low melting temperature (between 106 °C and 133 °C depending on thermal history[75]) and has been used in thermal energy storage applications.[76,77] The measurement and fitting methods were kept the same as the procedure used for the reference samples except that the ambient temperature was varied with the test setup inside a furnace and the hot-wire sensor had a protective coating layer (which was included in the model analysis). After reaching the desired measurement temperature, the sensor and the sample were held for 30 min to reach thermal equilibrium before starting measurements. Data were collected at 16 temperature points, and we found that the model gave good fits from the solid phase [Fig. 12(a)] through the liquid phase [Fig. 12(b)] and up to near the vaporization point [Fig. 12(c)]. The density[78] and heat capacity[79] of sulfur were used in the model to reduce fitting parameters. To ensure that sensors were not damaged during testing at high temperature in the sulfur environment, the room temperature electrical resistance of the Pt wire before and after the measurements was measured and found to be unchanged. This supports the durability of the protective $Al_2O_3$ coating for a measurement conducted at high temperature and the full temperature range. Additionally, after the high temperature cycling in sulfur, tests of the lower temperature thermal conductivity were repeated, and the deviation between pre- and post-high temperature results were within the measurement uncertainty. Due to potential longer-term corrosion of the coating during thermal cycling in molten sulfur, we did not reuse the sensors for high temperature tests. The batch processing and mass-producible nature of these sensors allow them to be easily replaced in cases when multiple high temperature measurements are desired.

蒸发点

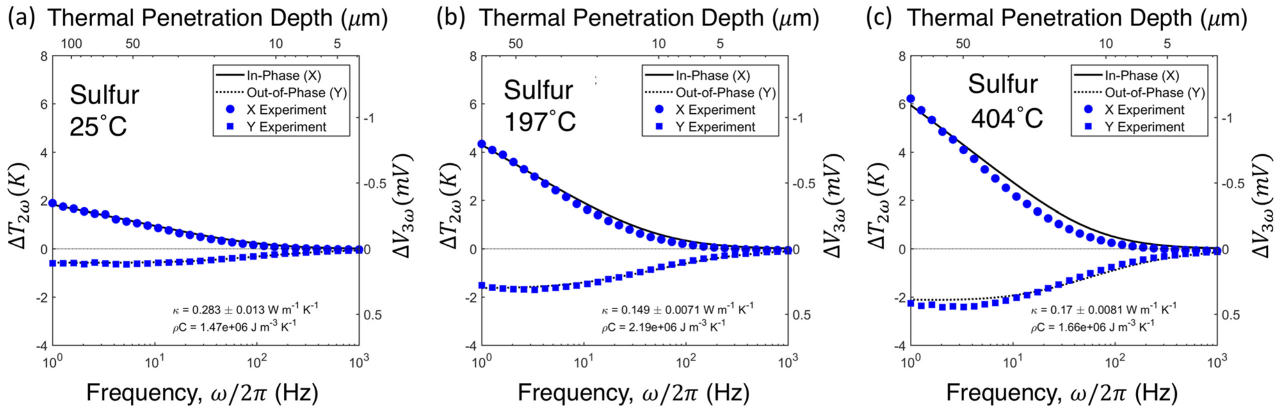

**FIG. 12**. Frequency sweeps for sulfur in (a) the solid phase, (b) the liquid phase, and (c) near the vaporization temperature. Measurement temperature, fitted thermal conductivity, and reference heat capacity are shown in each figure.

The fitted thermal conductivity from room temperature up to the vaporization point is shown in Fig. 13 and exhibits four distinct temperature zones. The first two are below ~140 °C with sulfur in its solid phase. From room temperature, sulfur is in an orthorhombic crystal phase, and the thermal conductivity monotonically decreases from ~0.28 W m$^{-1}$ K$^{-1}$, and then at ~100 °C, sulfur undergoes a transformation to a monoclinic crystal structure. This is accompanied by a sharp drop in the thermal conductivity to ~0.15 W m$^{-1}$ K$^{-1}$. This slightly increases with temperature until sulfur melts above ~135 °C for our system, where the thermal conductivity drops slightly lower again. Then, from 159 °C to 212 °C, sulfur undergoes polymerization,[75] where the sulfur rings begin to break apart and form long chains. This polymerization range includes a dramatic increase in the heat capacity,[79] and the thermal conductivity monotonically increases until the sulfur reaches a depolymerization[80] point, where the thermal conductivity plateaus and is a nearly constant ~0.17 W m$^{-1}$ K$^{-1}$ up to the vaporization temperature. It is nice to note that our measurements closely follow those from the literature for orthorhombic,[81–85] monoclinic,[84] and molten sulfur.[84,86] The most important aspect of this measurement, however, is that it shows that the measurement procedure (sensor design and data analysis) can function through solid and liquid phase transformation and is even sensitive enough to pick up changes in thermal properties due to solid–solid phase transformations in a reactive/corrosive material.

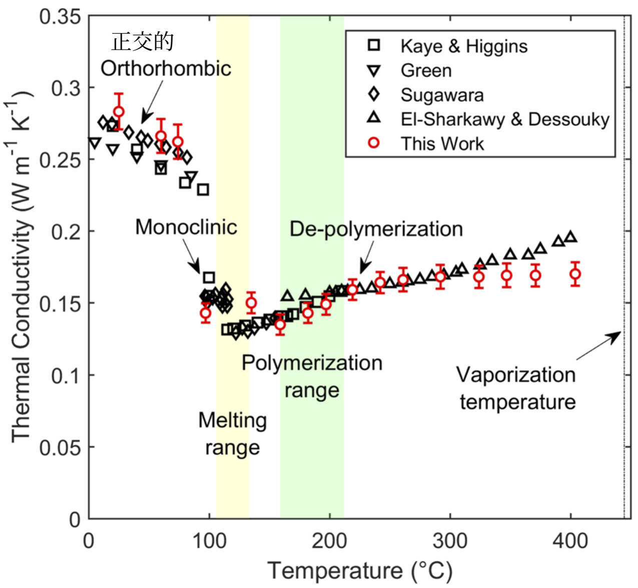

**FIG. 13**. Thermal conductivity of sulfur from room temperature up to near the vaporization point. Experimental measurements are shown in comparison to literature values.[81,82,84,86]

## VIII. CONCLUSION

To aid in the design of high-temperature energy systems and advanced manufacturing, we designed and fabricated sensors capable of measuring the thermal conductivity of high-temperature and reactive solids, fluids, and gases. We presented a full three-dimensional thermal model of our platinum hot-wire sensor, which accounts for both radial conduction into the sample and axial conduction along the wire including the effect of coating layers on the wire. This is the first time a frequency-domain hot-wire measurement has used a full three-dimensional multilayer thermal model, which has proven critical in providing accurate thermal conductivity value measurements. Measuring high-temperature fluids in the frequency domain eliminates inherent errors in time-domain measurements such as 1/f noise, ambient temperature fluctuations from the environment or furnace, and data truncation to avoid errors from the wire itself, convection, or the sample holder. We validated our frequency-domain hot-wire measurement and model by measuring the thermal conductivity of several standard fluids at room temperature with full error propagation analysis. After validating this measurement technique, we measured the thermal conductivity of sulfur from the solid phase through the melting point and just below the vaporization point to highlight the capability of the measurement system in a high temperature and reactive environment.

## ACKNOWLEDGMENTS

This paper is based on the work supported by the DOE Solar Energy Technologies Office under Grant No. DE-EE0001592. Los Alamos National Laboratory is a multimission laboratory managed and operated by Triad National Security, LLC, for the U.S. Department of Energy's National Nuclear Security Administration under Contract No. 89233218CNA000001. The document release number is Grant No. LA-UR-20-20559.

## REFERENCES

[1] V. M. B. Nunes, M. J. V. Lourenço, F. J. V. Santos, and C. A. Nieto de Castro, J. Chem. Eng. Data **48**(3), 446–450 (2003).

[2] M. Mehos, C. Turchi, J. Vidal, M. Wagner, Z. Ma, C. Ho, W. Kolb, C. Andraka and A. Kruizenga, "Concentrating Solar Power Gen3 Demonstration Roadmap," Office of Scientific and Technical Information (Oak Ridge, 2017).

[3] S. A. Wright, R. F. Radel, M. E. Vernon, G. E. Rochau, and P. S. Pickard, Sandia Report No. SAND2010-0171, 2010.

[4] B. D. Iverson, T. M. Conboy, J. J. Pasch, and A. M. Kruizenga, Appl. Energy **111**, 957–970 (2013).

[5] J. Serp, M. Allibert, O. Beneš, S. Delpech, O. Feynberg, V. Ghetta, D. Heuer, D. Holcomb, V. Ignatiev, J. L. Kloosterman, L. Luzzi, E. Merle-Lucotte, J. Uhlíř, R. Yoshioka, and D. Zhimin, Prog. Nucl. Energy **77**, 308–319 (2014).

[6] C. W. Forsberg, P. F. Peterson, and P. S. Pickard, Nucl. Technol. **144**(3), 289–302 (2003).

[7] K. Tuček, J. Carlsson, and H. Wider, Nucl. Eng. Des. **236**(14), 1589–1598 (2006).

[8] J. A. Eastman, S. R. Phillpot, S. U. S. Choi, and P. Keblinski, Annu. Rev. Mater. Res. **34**(1), 219–246 (2004).

[9] P. Keblinski, J. A. Eastman, and D. G. Cahill, Mater. Today **8**(6), 36–44 (2005).

[10] M. I. Pryazhnikov, A. V. Minakov, V. Y. Rudyak, and D. V. Guzei, Int. J. Heat Mass Transfer **104**, 1275–1282 (2017).

[11] S. Rashidi, O. Mahian, and E. M. Languri, J. Therm. Anal. Calorim. **131**(3), 2027–2039 (2018).

[12] L. Wang and S. Felicelli, Mater. Sci. Eng. **435-436**, 625–631 (2006).

[13] S. M. Thompson, L. Bian, N. Shamsaei, and A. Yadollahi, Addit. Manuf. **8**, 36–62 (2015).

[14] M. J. Assael, K. D. Antoniadis, and W. A. Wakeham, Int. J. Thermophys. **31**(6), 1051–1072 (2010).

[15] C. A. Nieto de Castro, J. C. G. Calado, W. A. Wakeham, and M. Dix, J. Phys. E: Sci. Instrum. **9**(12), 1073–1080 (1976).

[16] Y. Nagasaka and A. Nagashima, Rev. Sci. Instrum. **52**(2), 229–232 (1981).

[17] Y. Nagasaka and A. Nagashima, J. Phys. E: Sci. Instrum. **14**(12), 1435 (1981).

[18] H. Xie, H. Gu, M. Fujii, and X. Zhang, Meas. Sci. Technol. **17**(1), 208 (2006).

[19] W. Yu and S. U.-S. Choi, Rev. Sci. Instrum. **77**(7), 076102 (2006).

[20] M. Hoshi, T. Omotani, and A. Nagashima, Rev. Sci. Instrum. **52**(5), 755–758 (1981).

[21] X. Zhang and M. Fujii, Int. J. Thermophys. **21**(1), 71–84 (2000).

[22] M. V. Peralta-Martinez and W. A. Wakeham, Int. J. Thermophys. **22**(2), 395–403 (2001).

[23] E. Yamasue, M. Susa, H. Fukuyama, and K. Nagata, Int. J. Thermophys. **24**(3), 713–730 (2003).

[24] L. C. Wei, L. E. Ehrlich, M. J. Powell-Palm, C. Montgomery, J. Beuth, and J. A. Malen, Addit. Manuf. **21**, 201–208 (2018).

[25] W. T. Kierkus, N. Mani, and J. E. S. Venart, Can. J. Phys. **51**(11), 1182–1186 (1973).

[26] J. H. Blackwell, Can. J. Phys. **34**(4), 412–417 (1956).

[27] H. M. Roder, J. Res. Natl. Bur. Stand. **86**(5), 457–493 (1981).

[28] J. J. Healy, J. J. de Groot, and J. Kestin, Physica B+C **82**(2), 392–408 (1976).

[29] J. J. De Groot, J. Kestin, and H. Sookiazian, Physica **75**(3), 454–482 (1974).

[30] M. J. Assael, L. Karagiannidis, N. Malamataris, and W. A. Wakeham, Int. J. Thermophys. **19**(2), 379–389 (1998).

[31] G. Bran-Anleu, A. S. Lavine, R. E. Wirz, and H. P. Kavehpour, Rev. Sci. Instrum. **85**(4), 045105 (2014).

[32] D. G. Cahill, Rev. Sci. Instrum. **61**(2), 802–808 (1990).

[33] C. Dames and G. Chen, Rev. Sci. Instrum. **76**(12), 124902 (2005).

[34] T. Borca-Tasciuc, A. R. Kumar, and G. Chen, Rev. Sci. Instrum. **72**(4), 2139–2147 (2001).

[35] T. Tong and A. Majumdar, Rev. Sci. Instrum. **77**(10), 104902 (2006).

[36] M. L. Bauer and P. M. Norris, Rev. Sci. Instrum. **85**(6), 064903 (2014).

[37] N. O. Birge and S. R. Nagel, Phys. Rev. Lett. **54**(25), 2674–2677 (1985).

[38] N. O. Birge, Phys. Rev. B **34**(3), 1631–1642 (1986).

[39] N. O. Birge and S. R. Nagel, Rev. Sci. Instrum. **58**(8), 1464–1470 (1987).

[40] S. R. Choi, J. Kim, and D. Kim, Rev. Sci. Instrum. **78**(8), 084902 (2007).

[41] S. R. Choi and D. Kim, Rev. Sci. Instrum. **79**(6), 064901 (2008).

[42] S. Roy-Panzer, T. Kodama, S. Lingamneni, M. A. Panzer, M. Asheghi, and K. E. Goodson, Rev. Sci. Instrum. **86**(2), 024901 (2015).

[43] S. D. Lubner, J. Choi, G. Wehmeyer, B. Waag, V. Mishra, H. Natesan, J. C. Bischof, and C. Dames, Rev. Sci. Instrum. **86**(1), 014905 (2015).

[44] L. Lu, W. Yi, and D. L. Zhang, Rev. Sci. Instrum. **72**(7), 2996–3003 (2001).

[45] S.-M. Lee, Rev. Sci. Instrum. **80**(2), 024901 (2009).

[46] R. Heyd, A. Hadaoui, M. Fliyou, A. Koumina, L. E. H. Ameziane, A. Outzourhit, and M.-L. Saboungi, Rev. Sci. Instrum. **81**(4), 044901 (2010).

[47] R. Karthik, R. Harish Nagarajan, B. Raja, and P. Damodharan, Exp. Therm. Fluid Sci. **40**, 1–9 (2012).

[48] S. Kommandur, A. Mahdavifar, P. J. Hesketh, and S. Yee, Sens. Actuators, A **233**, 231–238 (2015).

[49] S. R. Atalla, A. A. El-Sharkawy, and F. A. Gasser, Int. J. Thermophys. **2**(2), 155–162 (1981).

[50] E. Yusibani, P. L. Woodfield, M. Fujii, K. Shinzato, X. Zhang, and Y. Takata, Int. J. Thermophys. **30**(2), 397–415 (2009).

[51] E. Yusibani, P. L. Woodfield, S. Moroe, K. Shinzato, M. Kohno, Y. Takata, and M. Fujii, J. Therm. Sci. Technol. **4**(1), 146–158 (2009).

[52] E. Yusibani, P. L. Woodfield, M. Kohno, K. Shinzato, Y. Takata, and M. Fujii, Int. J. Thermophys. **30**(3), 833–850 (2009).

[53] S. N. Schiffres and J. A. Malen, Rev. Sci. Instrum. **82**(6), 064903 (2011).

[54] S. Kommandur, A. Mahdavifar, S. Jin, P. J. Hesketh, and S. Yee, Sens. Actuators, A **250**, 243–249 (2016).

[55] K. D. Antoniadis, G. J. Tertsinidou, M. J. Assael, and W. A. Wakeham, Int. J. Thermophys. **37**(8), 78 (2016).

[56] Z. L. Wang, D. W. Tang, S. Liu, X. H. Zheng, and N. Araki, Int. J. Thermophys. **28**(4), 1255–1268 (2007).

[57] A. Turgut, I. Tavman, M. Chirtoc, H. P. Schuchmann, C. Sauter, and S. Tavman, Int. J. Thermophys. **30**(4), 1213–1226 (2009).

[58] S. Kakac and Y. Yener, *Heat Conduction* (University of Miami, Coral Gables, FL, 1985).

[59] C. S. Gorham, J. T. Gaskins, G. N. Parsons, M. D. Losego, and P. E. Hopkins, Appl. Phys. Lett. **104**(25), 253107 (2014).

[60] X. Wei, T. Zhang, and T. Luo, ACS Energy Lett. **2**(10), 2283–2292 (2017).

[61] O. M. Wilson, X. Hu, D. G. Cahill, and P. V. Braun, Phys. Rev. B **66**(22), 224301 (2002).

[62] Y. Heichal and S. Chandra, J. Heat Transfer **127**(11), 1269–1275 (2005).

[63] E. Chapelle, B. Garnier, and B. Bourouga, Int. J. Therm. Sci. **48**(12), 2221–2227 (2009).

[64] E. W. Lemmon and R. T. Jacobsen, Int. J. Thermophys. **25**(1), 21–69 (2004).

[65] O. Sandberg and B. Sundqvist, J. Appl. Phys. **53**(12), 8751–8755 (1982).

[66] G. Guevara-Carrion, C. Nieto-Draghi, J. Vrabec, and H. Hasse, J. Phys. Chem. B **112**(51), 16664–16674 (2008).

[67] J. Petravic, J. Chem. Phys. **123**(17), 174503 (2005).

[68] A. I. Krivchikov, A. N. Yushchenko, O. A. Korolyuk, F. J. Bermejo, C. Cabrillo, and M. A. González, Phys. Rev. B **75**(21), 214204 (2007).

[69] M. L. V. Ramires, C. A. Nieto de Castro, Y. Nagasaka, A. Nagashima, M. J. Assael, and W. A. Wakeham, J. Phys. Chem. Ref. Data **24**(3), 1377–1381 (1995).

[70] S. W. Hong, Y.-T. Kang, C. Kleinstreuer, and J. Koo, Int. J. Heat Mass Transfer **54**(15), 3448–3456 (2011).

[71] M. L. Huber, R. A. Perkins, D. G. Friend, J. V. Sengers, M. J. Assael, I. N. Metaxa, K. Miyagawa, R. Hellmann, and E. Vogel, J. Phys. Chem. Ref. Data **41**(3), 033102 (2012).

[72] R. P. Bhatta, S. Annamalai, R. K. Mohr, M. Brandys, I. L. Pegg, and B. Dutta, Rev. Sci. Instrum. **81**(11), 114904 (2010).

[73] J. W. Arblaster, Platinum Met. Rev. **50**(3), 118–119 (2006).

[74] J. W. Arblaster, Platinum Met. Rev. **49**(3), 141–149 (2005).

[75] B. Meyer, Chem. Rev. **76**(3), 367–388 (1976).

[76] P. D. Clark and N. I. Dowling, J. Sulfur Chem. **25**(1), 7–11 (2004).

[77] M. Shinn, K. Nithyanandam, A. Barde, and R. E. Wirz, Appl. Therm. Eng. **128**(Suppl. C), 1009–1021 (2018).

[78] P. Espeau and R. Céolin, Thermochim. Acta **459**(1), 127–129 (2007).

[79] E. D. West, J. Am. Chem. Soc. **81**(1), 29–37 (1959).

[80] G. C. Vezzoli, P. J. Kisatsky, L. W. Doremus, and P. J. Walsh, Appl. Opt. **15**(2), 327–339 (1976).

[81] G. W. C. Kaye and W. F. Higgins, Proc. R. Soc. London, Ser. A **122**(790), 633–646 (1929).

[82] S. E. Green, Proc. Phys. Soc. **44**(3), 295 (1932).

[83] Y. Yoshizawa, A. Sugawara, and E. Yamada, J. Appl. Phys. **35**(4), 1354–1355 (1964).

[84] A. Sugawara, J. Appl. Phys. **36**(8), 2375–2377 (1965).

[85] G. A. Slack, Phys. Rev. **139**(2A), A507–A515 (1965).

[86] A. A. El-Sharkawy and M. T. Dessouky, Int. J. Thermophys. **4**(2), 115–125 (1983).